Towards Real-time 3D Geometric Nonlinear Diffusion Filter and Its Application to CT and MR Imaging

Mohammad Arafat Hussain
Department of EEE, Eastern University
Dhaka–1205, Bangladesh
Email: arafat.eee@easternuni.edu.bd

Riad Mashrub Shourov
Directorate of Technical Education
Dhaka–1207, Bangladesh
Email: riadmashrub.shourov@gmail.com

Shamima Nasrin Khan
Department of IPE, BUET
Dhaka–1000, Bangladesh
Email: shnkeasha@gmail.com

Abstract—We propose two near real-time nonlinear anisotropic diffusion filtering (NADF) methods for the 2D and 3D X-ray computed tomography (CT) and magnetic resonance (MR) image denoising. Typically, NADFs are preferred for the medical image denoising due to its edge preserving feature though they are computationally expensive. Recently, a computation-time efficient 2D NADF has been proposed which uses local pixel intensity-based geometric parameters for diffusion. But it has limitations resulting from (i) its assumption that the neighboring pixels are non-noisy while deciding on an interrogated pixel being noisy or not, and (ii) its confinement of working only on a 2D image. Motivated from this, we propose an improved 2D NADF method that uses additional neighboring pixels in an effective way to lower the noise impact on the estimated geometric parameters. We also extend our 2D method into 3D that considers all the three directions for information diffusion. The performance of the proposed methods is evaluated using a 3D synthetic phantom, and *in vivo* CT and MR data which demonstrates an average signal-to-noise-ratio-gain improvement of approximately 58% in 2D and 96% in 3D phantom data, and approximately 79% in 2D and 127% in 3D *in vivo* data, compared to the state-of-the-art method.

Index Terms—Diffusion filter, computed tomography, magnetic resonance imaging.

I. INTRODUCTION

Typically medical images are of low contrast and often characterized with a complex type of noise. This noise can be introduced from acquisition systems, transmission storage, and display devices [1]. Noise in the X-ray computed tomography (CT) images is typically characterized by the Poisson distribution [2]. However, the Gaussian distribution can be used for the CT noise modeling as an accurate continuous approximation for the Poisson distribution [3], [4]. On the other hand, noise in a magnetic resonance (MR) image is fundamentally different than that of a CT image, and is characterized by the Rician distribution [1], [5]. But here also, for an MR image with high signal-to-noise ratio (SNR), the Rician noise pdf can be approximated by a Gaussian pdf [6], [7], [8]. Image denoising is very crucial in digital CT imaging as it may lead to reduced X-ray dose to patients without noticeable degradation of the image quality. Besides, MR imaging plays an important role in modern medical diagnosis and therapy because of their non-invasiveness, high-resolution and isotropic voxels, but often challenged by the noise that degrades the quality of an image.

To denoise both the CT and MR images, a number of methods have been developed, e.g., the Wiener filtering [9], Gaussian filtering [10], nonlinear anisotropic diffusion filtering (NADF) [11], total variation minimization [12], wavelet thresholding [13], and bilateral filter [14]. NADF is one of the most widely used denoising techniques in medical imaging, specially in the CT and MR imaging; due to its capability of preserving image features (e.g., anatomical edges) compared to other methods during a noise removing process [15]. However, NADF scheme needs large amount of computation for the calculation of diffusion coefficients and gradients at every pixel [16]. Recently, a geometric parameter-based 2D NADF model has been proposed to use in the X-ray image denoising [17]. It uses geometric parameters derived from the local pixel intensity distribution in calculating the diffusion coefficients in the horizontal and vertical directions rather than employing four directional gradients around the pixel of interest as traditionally used in NADF models [7], [11]. This filter [17] has shown better performance than those in [7], [11] in terms of edge preservation and noise reduction while the computation time has been greatly reduced. However, it also has some built-in limitations. Firstly, it assumes the neighboring pixels non-noisy while deciding on an interrogated pixel either it is noisy or not. This assumption is not always true since the whole image usually becomes corrupted by noise. And secondly, it is designed to work on a single 2D X-ray or CT or MR image slice. But since the CT and MR images are acquired in 3D volumes, and detailed spatial information of the images is stressed in all three directions, it is important to consider all three directions for information diffusion.

In this paper, we mitigate the limitations of the previously reported geometric parameter-based NADF method in [17] by proposing two effective methods for 2D and 3D near real-time geometric NADF for the CT and MR image denoising. Our improved 2D method considers additional neighboring pixels to reduce the noise impact on the geometric parameters which in turn allows the method not to rely on the assumption that the neighboring pixels are non-noisy as assumed in [17]. Finally,

we extend our improved 2D method into 3D that considers the whole 3D image volume at a time to estimate the geometric parameters rather than the 2D slice-by-slice approach adopted by González et al. [17]. The proposed 3D method takes the challenge of denoising a 3D image volume in near real-time which exploits the spatial information from all three directions. The performance of the proposed methods is evaluated using the 3D synthetic phantom, and *in vivo* CT and MR data.

This paper is organized as follows. Section II presents an overview of the geometric NADF method [17], and subsequently the proposed methods in detail. Section III presents the simulation and experimental results to demonstrate the strength of the proposed algorithms. Concluding remarks are presented in Section IV.

II. METHODS

A. Overview of the Traditional 2D Geometric NADF (T2DF)

Typically, in detecting an edge along a line of intensity pixels on a 2D image grid, we may face two types of pixels: the noise pixel and edge pixel (see Fig. 1). A noise pixel is one which has much higher or lower intensity than the adjacent pixels having similar intensities. The edge pixel is one which is either on an inclining or declining slope. Using these topologies, González et al. [17] defined the following parameters:
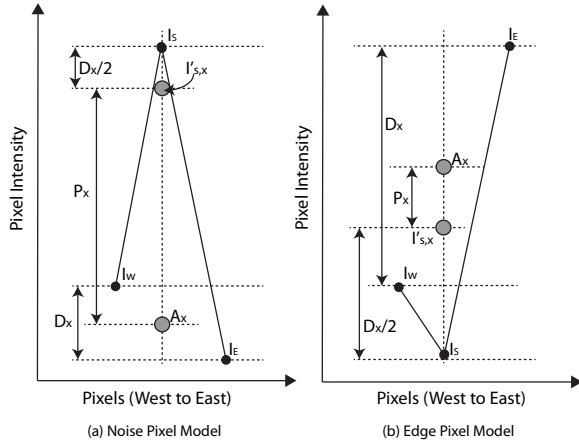

Fig. 1. Representation of a typical (a) noise pixel and (b) edge pixel.

$$A_X = \frac{1}{2}(I_E + I_W), \tag{1}$$

$$D_x = \begin{cases} \mid \nabla_E - \nabla_W \mid -\delta & \text{if } \mid \nabla_E - \nabla_W \mid > \delta \\ 0 & \text{otherwise,} \end{cases} \tag{2}$$

$$I'_{s,x} = \begin{cases} I_s - \frac{1}{2}D_X & \text{if } I_s > A_X \\ I_s + \frac{1}{2}D_X & \text{if } I_s \leq A_X, \end{cases} \tag{3}$$

$$P_X = I'_{s,x} - A_X, \tag{4}$$

where I_E and I_W represent the image intensity values at the East (E) and West (W) neighboring pixels, A_X represents the

average of the neighboring pixels in the $x-$direction (E-W), $\nabla_P = I_P - I_s$, ($P = E$ and W), and I_s is the intensity value of the interrogated pixel. An auxiliary parameter $\delta \in [0, \sigma]$ is defined to prevent small noise regions to be identified as edges, where σ is the standard deviation of the image noise. In [17], median absolute deviation is used for automatic computation of δ. For the $y-$direction (North (N)-South (S)), similar parameters D_Y, A_Y, $I'_{s,y}$, and P_Y are estimated. Then the diffusivity function along the E-W and N-S directions, respectively, are defined as [17]

$$\begin{aligned} c(D_X, P_X) &= \frac{1}{1+(D_X/P_X)^2}, \\ c(D_Y, P_Y) &= \frac{1}{1+(D_Y/P_Y)^2}. \end{aligned} \tag{5}$$

Finally, the geometric NADF is defined as [17]

$$\begin{aligned} I_s^{t+\triangle t} &= I_s^t + \triangle t \times [c(D_X, P_X) \cdot (\nabla_E + \nabla_W) \\ &+ c(D_Y, P_Y) \cdot (\nabla_N + \nabla_S)]^t, \end{aligned} \tag{6}$$

where $\triangle t$ is the time step in each iteration.

B. Improved 2D Geometric NADF

To mitigate the first limitation of the T2DF method, we consider the rest of the neighboring pixels I_{NE}, I_{NW}, I_{SE} and I_{SW} along with I_E, I_W, I_N and I_S pixels to estimate the parameters D_X, $I'_{s,x}$ and P_X in Eqns. (2)-(4) so that the impact of the corrupted neighboring pixels become lesser than that of the traditional way. However, an universal limitation of using information from a greater number of directions is that the step size $\triangle t$ cannot be greater than $1/2d$ in order to fulfill the stability requirement of a discretized diffusion filtering process [16], [17], where d is the number of directions along which the gradients/intensity parameters are calculated. Using two additional directional (i.e., North east (NE)-South west (SW) and North west (NW)-South east (SE)) information on a 2D image grid causes $\triangle t$ become much smaller which results in smaller amount of information flow in each iteration. Consequently, the computation time is expected to be increased considerably compared to the T2DF method to perform the similar noise reduction as that by the T2DF method.

Considering all the limiting factors above, we devise a simple but very effective way of using four directions (i.e., E-W, N-S, NS-SW and NW-SE) for information flow while $\triangle t$ still holds the value for only two directions (i.e., E-W and N-S). We estimate ∇_E, ∇_W, ∇_N and ∇_S differently than that in the T2DF method by using the mean intensities of one-sided neighboring pixels as

$$\begin{aligned} \nabla_E &= \frac{I_{NE}+I_E+I_{SE}}{3} - I_s, \\ \nabla_W &= \frac{I_{NW}+I_W+I_{SW}}{3} - I_s, \\ \nabla_N &= \frac{I_{NE}+I_N+I_{NW}}{3} - I_s, \\ \nabla_S &= \frac{I_{SE}+I_S+I_{SW}}{3} - I_s. \end{aligned} \tag{7}$$

We use these modified ∇_E, ∇_W, ∇_N and ∇_S values into Eqns. (1)-(6) to improve the T2DF method which we call the improved 2D geometric NADF (IM2DF) method.
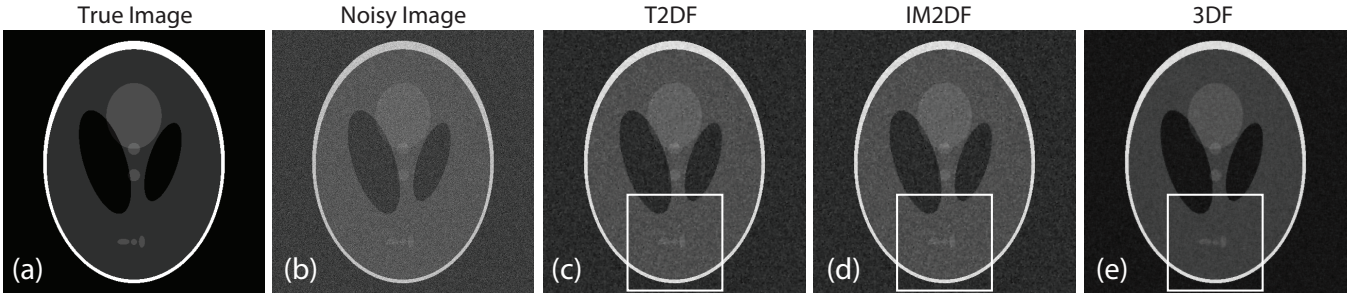
Fig. 2. Illustration of the diffusion filtering performances using the synthetic data. (a) A slice from the true phantom image volume. (b) A slice from the corrupted phantom image volume with the additive white Gaussian noise of standard deviation 0.0036 (SNR = 5dB), and the same slice is filtered by (c) the T2DF, (d) IM2DF, and (e) 3DF methods. In all the cases, the number of iterations = 3.

C. 3D Geometric NADF

Finally, to mitigate the second limitation of the T2DF method, we propose a 3D geometric NADF (3DF) by extending our IM2DF method into 3D. Typically, a 3D NADF scheme needs large amount of computation for the calculation of diffusion coefficients and gradients for every voxel in all three directions. In our proposed 3DF method, we exploit the same concept of estimating the diffusivity functions as in the IM2DF method which saves a large amount of computation time. In addition, the proposed 3DF method considers the whole 3D image volume to estimate $\delta \in [0, \sigma]$ rather than each individual 2D slice as in [17]. We estimate parameters A_Z, D_Z, $I'_{s,z}$, and P_Z for the elevation direction (i.e., the direction perpendicular to the E-W-N-S plane) using Eqns. (1)-(4) and (7). Then the diffusivity function along the elevation direction is defined as

$$c(D_Z, P_Z) = \frac{1}{1 + (D_Z/P_Z)^2}. \qquad (8)$$

Finally, the discrete implementation of the 3DF is defined as

$$
\begin{aligned}
I_s^{t+\triangle t} &= I_s^t + \triangle t \times [c(D_X, P_X) \cdot (\nabla_E + \nabla_W) \\
&+ c(D_Y, P_Y) \cdot (\nabla_N + \nabla_S) \\
&+ c(D_Z, P_Z) \cdot (\nabla_T + \nabla_B)]^t, \qquad (9)
\end{aligned}
$$

where T and B denotes the top and bottom neighbors of the I_s voxel along the elevation direction, respectively.

III. RESULTS

We provide comparative results of our proposed IM2DF and 3DF methods with the T2DF method [17] using the synthetic Shepp-Logan head phantom, and *in vivo* CT and MR data. We also compare the performance of different methods in terms of numerical metrics: signal-to-noise-ratio-gain (SNRG) [17] and mean structural similarity (MSSIM) [18]. We use four different SNR values (1, 5, 10 and 15dB) while adding the Gaussian noise to the data to analyze the SNRG and MSSIM performance. For consistency analysis, we use 100 realizations of each of the data sets at each SNR. The SNRG is evaluated for a uniform-intensity ROI on a single image slice as SNRG $= \frac{SNR_f}{SNR_n}$, where SNR_f and SNR_n are the SNR values in the filtered and true images, respectively. On the other hand, typically it is assumed that

the human visual perception is highly adapted for extracting structural information from a scene. The MSSIM is shown to be an excellent predictor of the image perceptual quality. It considers contrast, luminance and structural similarity between the filtered and true images to compute the value of the index. So, as closer the MSSIM index to the unity is, more visually closer the filtered and true images are. Due to space limitation, we do not provide the detail description of the MSSIM estimation process in this paper. Note that we refer the original machine acquired *in vivo* images as true images in this paper. Also note that we use $\triangle t$ = 0.25 and 0.16 for the 2D and 3D filtering approaches, respectively, and to filter the 3D image volumes with the 2D methods (i.e., T2DF and IM2DF), we perform filtering slice-by-slice individually.

A. Synthetic Data Results

To show the efficacy of our proposed methods, we use a 3D Shepp-Logan head phantom image of $512 \times 512 \times 16$ voxels [19]. We show a true image of a single slice of the 3D Shepp-Logan phantom in Fig. 2(a). We also show the noisier (SNR = 5dB) version of the same slice in Fig. 2(b). The 2D image slices (of 3D volumes) filtered by the T2DF, IM2DF and 3DF methods are shown in Figs. 2(c), (d) and (e), respectively. We see that the proposed IM2DF method better removes the grainy noise from the image than the T2DF method. In addition, the 3DF method performs the best among all the methods by producing more smooth image while preserving the image features (e.g., edges) at the same time. Our claim can be better realized from Fig. 3 where we show the magnified versions of the rectangular regions in Figs. 2(c)-(e).
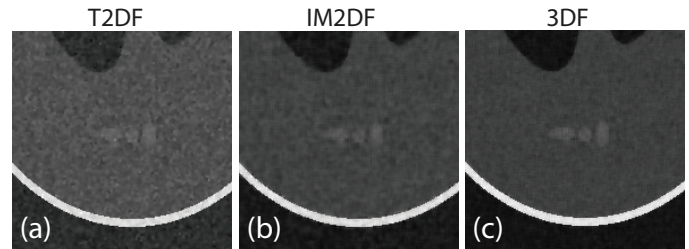

Fig. 3. Magnified illustration of the rectangular regions in Figs. 2(c)-(e) for the (a) T2DF, (b) IM2DF, and (c) 3DF methods.

TABLE I
ESTIMATED SNRG AT DIFFERENT SNR VALUES FOR THE T2DF, IM2DF
AND 3DF METHODS USING THE SHEPP-LOGAN HEAD PHANTOM

SNR =	1dB	5dB	10dB	15dB
T2DF	3.13±1.48	3.12±1.33	3.09±1.39	3.15±1.19
IM2DF	4.98±1.13	4.85±1.19	4.89±1.07	4.91±0.89
3DF	6.23±0.45	6.13±0.39	6.02±0.51	6.18±0.41

TABLE II
ESTIMATED MSSIM AT DIFFERENT SNR VALUES FOR THE T2DF, IM2DF
AND 3DF METHODS USING THE SHEPP-LOGAN HEAD PHANTOM

SNR =	1dB	5dB	10dB	15dB
T2DF	0.68±0.25	0.83±0.19	0.93±0.13	0.97±0.09
IM2DF	0.83±0.16	0.92±0.12	0.97±0.08	0.98±0.05
3DF	0.90±0.15	0.96±0.08	0.98±0.04	0.99±0.01

We also demonstrate the quantitative performance comparisons of the T2DF, IM2DF and 3DF methods in terms of the SNRG and MSSIM in Tables I and II, respectively. In Table I, we see that the mean SNRG values produced by the IM2DF method are greater than those of the T2DF method at all the SNR values. In addition, the 3DF method outperforms all other methods by producing the highest mean SNRG values at all the SNRs. Similarly, we see in Table II that the mean MSSIM values produced by the IM2DF method are greater than those of the T2DF method, and the 3DF method outperforms all other methods by producing the highest mean MSSIM values at all the SNR values. In addition, the estimated standard deviation values for both the SNRG and MSSIM metrics are lower, higher and the highest for the 3DF, IM2DF and T2DF methods, respectively, at all four SNR values.

B. In Vivo Data Results

1) Filtering of the CT Images: To illustrate the efficacy of our proposed methods with respect to the T2DF method, we use two sets of 3D CT image volumes (see Figs. 4 and 5) which are available in [20] to use in the research related purposes. In Figs. 4(a) and 5(a), we show the transverse view

TABLE III
ESTIMATED SNRG AT DIFFERENT SNR VALUES FOR THE T2DF, IM2DF
AND 3DF METHODS USING THE CT IMAGE VOLUME SETS-I AND II

Set	SNR =	1dB	5dB	10dB	15dB
I	T2DF	2.71±1.23	2.81±1.29	2.81±1.34	2.77±1.19
	IM2DF	5.08±1.03	5.01±1.07	5.17±0.96	5.00±1.13
	3DF	6.42±0.38	6.39±0.41	6.38±0.55	6.36±0.47
II	T2DF	2.73±1.38	2.53±1.13	2.72±1.28	2.92±1.18
	IM2DF	4.94±0.90	4.58±1.01	5.04±1.03	5.26±0.99
	3DF	6.41±0.47	6.09±0.44	6.35±0.52	6.31±0.51

TABLE IV
ESTIMATED MSSIM AT DIFFERENT SNR VALUES FOR THE T2DF, IM2DF
AND 3DF METHODS USING THE CT IMAGE VOLUME SETS-I AND II

Set	SNR =	1dB	5dB	10dB	15dB
I	T2DF	0.33±0.21	0.47±0.18	0.58±0.15	0.66±0.12
	IM2DF	0.40±0.15	0.51±0.12	0.61±0.10	0.73±0.08
	3DF	0.47±0.09	0.55±0.07	0.64±0.07	0.78±0.05
II	T2DF	0.67±0.38	0.70±0.33	0.81±0.29	0.90±0.19
	IM2DF	0.76±0.30	0.80±0.27	0.87±0.21	0.93±0.13
	3DF	0.80±0.23	0.88±0.18	0.93±0.12	0.97±0.07

TABLE V
ESTIMATED SNRG AT DIFFERENT SNR VALUES FOR THE T2DF, IM2DF
AND 3DF METHODS USING THE MR IMAGE VOLUME SETS-I AND II

Set	SNR =	1dB	5dB	10dB	15dB
I	T2DF	2.74±1.21	2.88±1.31	3.09±1.31	3.20±1.22
	IM2DF	4.97±1.07	4.78±1.11	5.46±0.98	5.32±1.15
	3DF	6.24±0.40	6.30±0.39	6.40±0.53	6.25±0.53
II	T2DF	2.50±1.42	2.70±1.16	2.52±1.26	2.52±1.21
	IM2DF	4.69±0.95	4.93±1.11	4.71±1.13	4.04±0.96
	3DF	5.93±0.43	6.03±0.41	5.98±0.48	5.29±0.53

TABLE VI
ESTIMATED MSSIM AT DIFFERENT SNR VALUES FOR THE T2DF, IM2DF
AND 3DF METHODS USING THE MR IMAGE VOLUME SETS-I AND II

Set	SNR =	1dB	5dB	10dB	15dB
I	T2DF	0.28±0.19	0.44±0.16	0.49±0.19	0.59±0.15
	IM2DF	0.33±0.14	0.45±0.15	0.55±0.13	0.68±0.11
	3DF	0.38±0.07	0.49±0.06	0.62±0.08	0.75±0.08
II	T2DF	0.62±0.43	0.71±0.37	0.82±0.32	0.90±0.21
	IM2DF	0.69±0.33	0.75±0.29	0.86±0.25	0.94±0.18
	3DF	0.72±0.21	0.83±0.15	0.93±0.13	0.97±0.09

slices from two sets of true CT image volumes acquired around the human pelvic and chest regions, respectively. These volumes are then corrupted with the additive white Gaussian noise of standard deviation 0.0036, of which two slices are shown in Figs. 4(b) and 5(b). These corrupted image volumes are then filtered by the T2DF, IM2DF and 3DF methods; corresponding single slices are shown in Figs. 4(c) and 5(c), 4(d) and 5(d), and 4(e) and 5(e), respectively. Similar to the phantom results, we see from these figures that the proposed IM2DF method better removes the grainy noise from the images than the T2DF method (see Figs. 4(c), (d) and 5(c), (d)). In addition, the 3DF method performs the best among all the methods by producing more smooth images while preserving the image features (see Figs. 4(e) and 5(e)).

Similar to the phantom results, we also demonstrate the quantitative performance comparisons of the T2DF, IM2DF and 3DF methods in terms of the SNRG and MSSIM in Tables III and IV, respectively, using the CT image sets-I and II. In Table III, we see that the mean SNRG values produced by the IM2DF are greater than those of the T2DF method at all the four noise powers for both the data sets. In addition, the 3DF method outperforms all other methods by producing the highest mean SNRG values at all the cases. Similarly, we see in Table IV that the mean MSSIM values produced by the IM2DF are greater than those of the T2DF method, and the 3DF method outperforms all other methods by producing the highest mean MSSIM values at all the four noise powers for both the data sets. In addition, the estimated standard deviation values for both the SNRG and MSSIM metrics are lower, higher and the highest for the 3DF, IM2DF and T2DF methods, respectively, at all the cases.

2) Filtering of the MR Images: In addition to the filtering performance evaluation using the CT image volumes, we also demonstrate the efficacy of our proposed methods with respect to the T2DF method using two sets of 3D MR image volumes available in [20] (see Figs. 6 and 7). In Figs. 6(a) and 7(a),
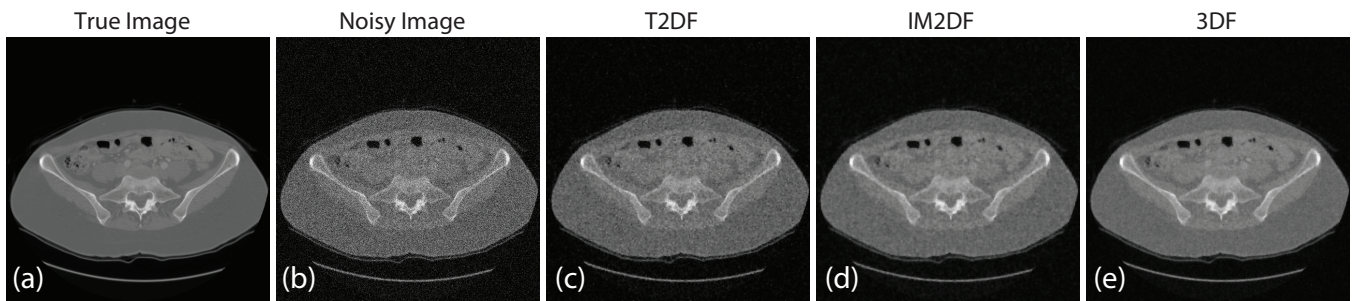
Fig. 4. Illustration of the diffusion filtering performances using the *in vivo* CT image set-I. (a) A slice (transverse view) from the true CT image volume captured around the human pelvic region. (b) A slice from the corrupted image volume with the additive white Gaussian noise of standard deviation 0.0036 (SNR = 5dB), and the same slice is filtered by (c) the T2DF, (d) IM2DF, and (e) 3DF methods. In all the cases, the number of iterations = 3.
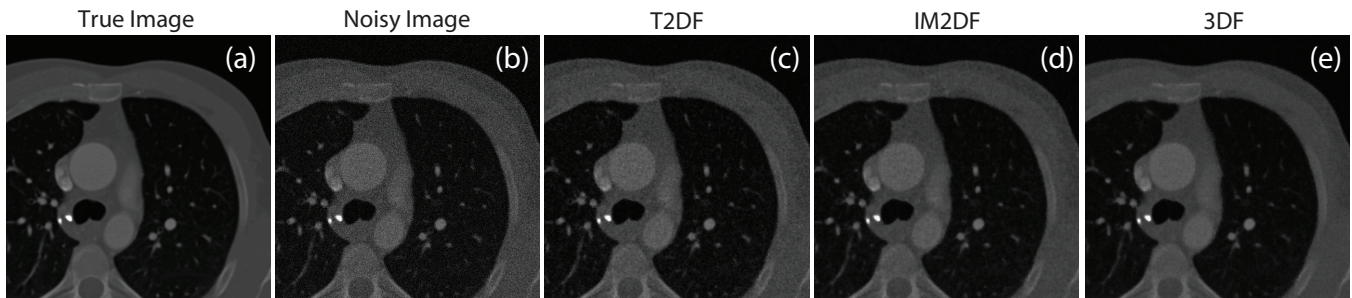

Fig. 5. Illustration of the diffusion filtering performances using the *in vivo* CT image set-II. (a) A slice (transverse view) from the true CT image volume captured around the human chest (cardiac) region. (b) A slice from the corrupted image volume with the additive white Gaussian noise of standard deviation 0.0036 (SNR = 5dB), and the same slice is filtered by (c) the T2DF, (d) IM2DF, and (e) 3DF methods. In all the cases, the number of iterations = 3.
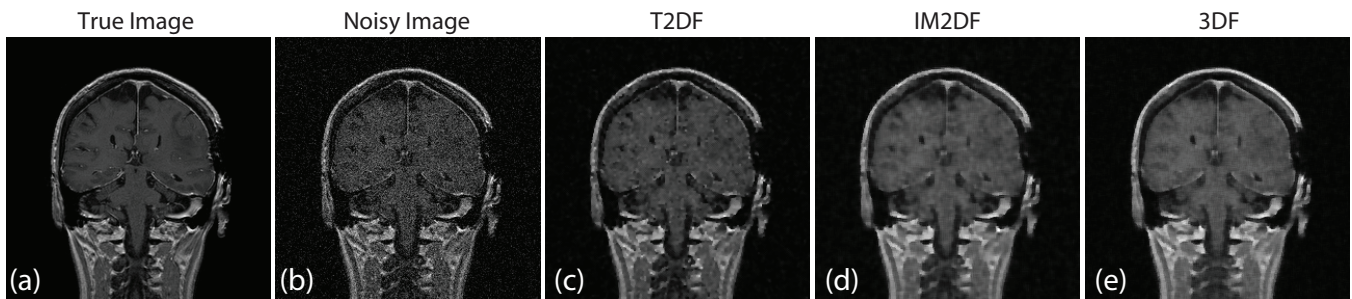

Fig. 6. Illustration of the diffusion filtering performances using the *in vivo* MR image (T1-weighted) set-I. (a) A slice (coronal view) from the true MR image volume captured around the human head-neck region. (b) A slice from the corrupted image volume with the additive white Gaussian noise of standard deviation 0.0036 (SNR = 5dB), and the same slice is filtered by (c) the T2DF, (d) IM2DF, and (e) 3DF methods. In all the cases, the iterations number = 3.
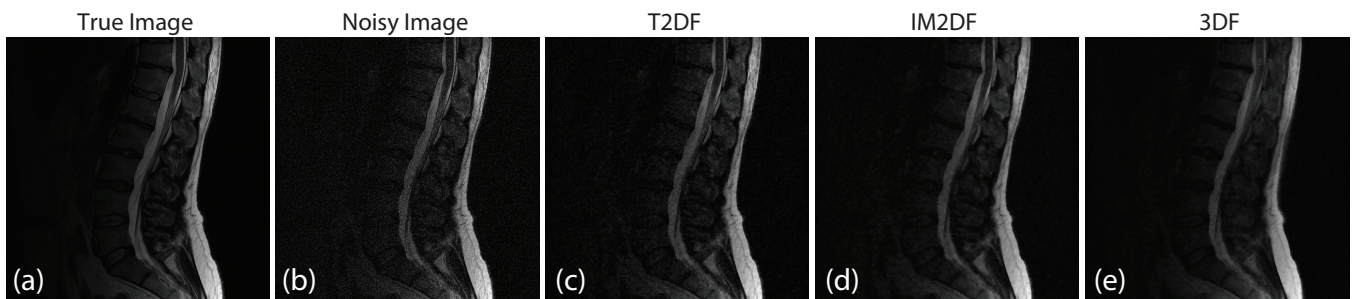

Fig. 7. Illustration of the diffusion filtering performances using the *in vivo* MR image (T2-weighted) set-II. (a) A slice (sagittal view) from the true MR image volume captured around the human lumber-spine region. (b) A slice from the corrupted image volume with the additive white Gaussian noise of standard deviation 0.0036 (SNR = 5dB), and the same slice is filtered by (c) the T2DF, (d) IM2DF, and (e) 3DF methods. In all the cases, the iterations number = 3.

we show the coronal and sagittal view slices from a T1- and T2-weighted true MR image volumes acquired around

the human head-neck and lumber-spine regions, respectively. These volumes are then corrupted with the additive white Gaussian noise of standard deviation 0.0036, of which two slices are shown in Figs. 6(b) and 7(b). These corrupted image volumes are then filtered by the T2DF, IM2DF and 3DF methods; corresponding single slices are shown in Figs. 6(c) and 7(c), 6(d) and 7(d), and 6(e) and 7(e), respectively. Similar to the CT image results, we see from these figures that the proposed IM2DF method better cleans the images than the T2DF method (see Figs. 6(c), (d) and 7(c), (d)). In addition, the 3DF method outperforms rest of the methods by producing more smooth images while preserving the image features at the same time (see Figs. 6(e) and 7(e)).

We also demonstrate the quantitative performance comparisons of the T2DF, IM2DF and 3DF methods in terms of the SNRG and MSSIM in Tables V and VI, respectively, using the MR image sets-I and II. Similar to the CT image results, we see that the mean SNRG values produced by the IM2DF are greater than those of the T2DF method at all the four noise powers for both the data sets (see Table V). In addition, the 3DF method outperforms all other methods by producing the highest mean SNRG values at all the four noise powers for both the data sets. Similarly, we see in Table VI that the mean MSSIM values produced by the IM2DF are greater than those of the T2DF method, and the 3DF method outperforms all other methods by producing the highest mean MSSIM values at all the cases. In addition, the estimated standard deviation values for both the SNRG and MSSIM metrics are lower, higher and the highest for the 3DF, IM2DF and T2DF methods, respectively, at all four SNR values for both the data sets as evident in Tables V and VI.

C. Computation Time

We estimated the computation time on a personal computer with a CPU: Intel(R) Core(TM) i5 @ 2.40GHz, Memory: 4GB. The filters have been implemented using the MATLAB (The Mathworks, Inc., Natic, MA.) and the computation time is evaluated excluding the data readout time from the disk to the PC memory. Considering a single iteration, the computation times by the Perona-Malik NADF [11], Weikert NADF [16], T2DF, IM2DF and 3DF methods for generating a filtered image (of size $512 \times 512 \times 1$ voxels) are 0.95, 1.25, 0.51, 0.61, and 0.65s, respectively.

IV. CONCLUSIONS

In this paper, we proposed two effective methods for 2D and 3D near real-time geometric nonlinear diffusion filtering for the CT and MR image denoising. Our improved 2D method considered additional neighboring pixels to reduce the noise impact on the geometric parameters which in turn allowed the method not to rely on the non-noisy neighboring pixels assumption as assumed in [17]. We also extended our improved 2D method into 3D that considered the whole 3D image volume at a time to estimate the geometric parameters so that it can exploit the spatial information from all three directions. The performance of the proposed methods was evaluated using the 3D synthetic phantom, and *in vivo* CT and MR data. Our test on the phantom data reported an average improvement of approximately 58% and 96% in terms of the SNRG, and 9% and 13% in terms of the MSSIM by the IM2DF and 3DF methods, respectively, compared to the state-of-the-art method. In addition, our test on the *in vivo* CT and MR data demonstrated an average improvement of approximately 79% and 127% in terms of the SNRG, 10% and 18% in terms of the MSSIM by the IM2DF and 3DF methods, respectively, compared to the state-of-the-art method. Although there is a little increment of the computation times for the IM2DF and 3DF methods compared to the T2DF method, these single iteration run-times are still below 1s and thus, we believe that the graphics processing unit-based implementation of these methods shall accelerate the execution time of these methods to real-time.

REFERENCES

[1] H. Gudbjartsson and S. Patz, "The Rician distribution of noisy MRI data," *Magn. Reson. Med.*, vol. 34, pp. 910–914, 1995.

[2] B. R. Whiting, P. Massoumzadeh, O. A. Earl, J. A. O'Sullivan, D. L. Snyder, and J. F. Williamson, "Properties of preprocessed sinogram data in x-ray computed tomography," *Med. Phys.*, vol. 33, no. 9, pp. 3290–3303, 2006.

[3] O. J. Tretiak, "Noise limitations in X-ray computed tomography," *J. Comput. Assisted Tomogr.*, vol. 2, pp. 477–480, 1978.

[4] J. Kalifa, A. F. Laine, and P. D. Esser, "Regularization in tomographic reconstruction using thresholding estimators," *IEEE Trans. Med. Imag.*, vol. 22, no. 3, pp. 351–359, 2003.

[5] A. Macovski, "Noise in MRI," *Magn. Reson. Med.*, vol. 36, pp. 494–497, 1996.

[6] R. D. Nowak, "Wavelet-based Rician noise removal for magnetic resonance imaging," *IEEE Trans. Imag. Process.*, vol. 8, no. 10, pp. 1408–1419, 1999.

[7] P. Bao and L. Zhang, "Noise reduction for magnetic resonance images via adaptive multiscale products thresholding," *IEEE Trans. Med. Imag.*, vol. 22, no. 9, pp. 1089–1099, 2003.

[8] H. Rabbani, R. Nezafat, and S. Gazor, "Wavelet-domain medical image denoising using bivariate laplacian mixture model," *IEEE Trans. Biomed. Engg.*, vol. 56, no. 12, pp. 2826–2837, 2009.

[9] N. Wiener, "Extrapolation, interpolation, and smoothing of stationary time series," *New York: Wiley*, 1949.

[10] M. Lindenbaum, M. Fischer, and A. Bruckstein, "On Gabor contribution to image enhancement," *Pattern Recogn.*, pp. 1–8, 1994.

[11] P. Perona and J. Malik, "Scale-space and edge detection using anisotropic diffusion," *IEEE Trans. Pattern Anal. Mach. Intell.*, vol. 12, pp. 629–39, 1990.

[12] L. I. Rudin, S. Osher, and E. Fatemi, "Nonlinear total variation based noise removal algorithms," *Physica D.*, vol. 60, pp. 259–68, 1992.

[13] D. L. Donoho, "De-noising by soft-thresholding," *IEEE Trans. Inform. Theory*, vol. 41, pp. 613–27, 1995.

[14] C. Tomasi and R. Manduchi, "Bilateral filtering for gray and color images," In: *6th Int. Conf. Comput. Vis.*, pp. 839–846, 1998.

[15] Y. Yongjian and S. T. Acton, "Speckle reducing anisotropic diffusion," *IEEE Trans. Image Process.* vol. 11, pp. 1260–1270, 2002.

[16] J. Weickert, B. M. Romeny, and M. A. Viergever, "Efficient and reliable schemes for nonlinear diffusion filtering," *IEEE Trans. Image Process.*, vol. 7, pp. 398–410, 1998.

[17] E. Michel-González, M. H. Cho, and S. Y. Lee, "Geometric nonlinear diffusion filter and its application to X-ray imaging," *BioMed. Eng. OnLine*, vol. 10:47, 2011.

[18] Z. Wang, A. C. Bovik, H. R. Sheikh, and E. P. Simoncelli, "Image Quality Assessment: From Error Visibility to Structural Similarity," *IEEE Trans. Image Process.*, vol. 13, no. 4, pp. 600–612, 2004.

[19] L. A. Shepp and B. F. Logan, "The Fourier reconstruction of a head section," *IEEE Trans. Nucl. Sci.*, vol. 21, pp. 21–34, 1974.

[20] URL: "http://www.osirix-viewer.com/datasets/," accessed on August 10, 2015.